International Journal of Mechanical Sciences 287 (2025) 109928

Contents lists available at ScienceDirect

International Journal of Mechanical Sciences

journal homepage: www.elsevier.com/locate/ijmecsci

Structural galloping suppression with high-frequency flutter

Liwei Dong [a,b,1], Chaoyang Zhao [a,1], Shuai Qu [a,b], Wei Ding [a,c], Guobiao Hu [d], Chengjia Han [a,*], Yaowen Yang [a,*]

[a] School of Civil and Environmental Engineering, Nanyang Technological University, 50 Nanyang Avenue, Singapore 639798, Singapore
[b] College of Transportation, Tongji University, Shanghai 201804, China
[c] School of Mechanical Engineering, Xi'an Jiaotong University, Xi'an, Shaanxi 710049, China
[d] Internet of Things Thrust, The Hong Kong University of Science and Technology (Guangzhou), Nansha, Guangzhou, Guangdong 511400, China

ARTICLE INFO

Keywords:
Passive vibration control
Flow-induced vibration
Structural galloping
High-frequency flutter
Excitation injection
Variable wind speed

ABSTRACT

Galloping presents a significant challenge in engineering, often causing large-amplitude vibrations in structures such as suspended electrical cables, bridges and towers, posing substantial risks and property damage. While injecting high-frequency excitations can mitigate structural galloping, current active suppression methods, which apply excitations after galloping has developed, are suboptimal, limiting their widespread adoption. In this study, a low-cost and easy-to-implement passive galloping suppression approach utilizing flutter-induced vibrations is proposed, exhibiting robust anti-galloping effects under natural wind conditions. By strategically placing flags, high-frequency fluttering forces generated by wind flow are exploited to impose surface loads on the structure rapidly. This preemptively suppresses low-frequency galloping, mitigating its onset effectively without necessitating substantial force. A distributed aerodynamic model is developed to simulate the suppression phenomenon, accompanied by a comprehensive analysis considering factors such as flutter characteristics, wind speed, and flag position and geometric parameters. The analysis also explores distinct suppression mechanisms that arise when the fluttering frequency approaches the second and third modal frequencies of the structure. The proposed galloping suppression approach has been successfully simulated and validated through theoretical calculations and experimental tests, and test results showcase a significant reduction in vibration amplitudes, with suppression ratios ranging from 85% to 95% across wind speeds of 3 m/s to 10 m/s. Additionally, this approach demonstrates effective suppression capabilities under variable wind speed conditions, indicating its reliability and practicality for mitigating detrimental galloping in real-world scenarios.

1. Introduction

Flow-induced vibration is a prevalent physical phenomenon arising from the interaction between fluid flow and slender structures, causing structural vibrations [1–3]. Depending on specific initiating conditions and characteristics, flow-induced vibrations (FIVs) can be categorized into several types, including vortex-induced vibration [4–6], flutter [7–9], galloping [10–12], and wake galloping [13–15]. Commonly observed in natural environments, FIVs impact a variety of flexible structures, such as plates [16,17], flags [18,19], towers [20,21], catenary risers [22], cables [23,24] and bridges [25–27]. However, they are considered detrimental in most natural environment, as lead to significant property damage and pose safety hazards [28–30].

Galloping is a type of self-excited large-amplitude oscillation that occurs at high wind velocities [31–33]. The underlying mechanism is attributed to asymmetric aerodynamic forces that develop on bodies with specific shapes (commonly square [34], triangular [35], and D-shape cross-sections [36,37]) or particular orientations relative to the flow. These forces generate restoring torques that are misaligned with the center of mass, causing the oscillation of the body. The oscillation amplitude increases if the structure's natural frequency closely matches the vortex shedding frequency or if aerodynamic forces increase with deflection in a particular manner. For galloping oscillations to persist, the wind velocity must exceed a critical threshold known as the cut-in speed [38–40]. Below this threshold, the energy imparted to the oscillating structure by the flow is insufficient to counteract the energy losses

* Corresponding authors.
E-mail addresses: chengjia.han@ntu.edu.sg (C. Han), cywyang@ntu.edu.sg (Y. Yang).
[1] These authors contribute equally to this study.

https://doi.org/10.1016/j.ijmecsci.2025.109928
Received 31 July 2024; Received in revised form 19 December 2024; Accepted 1 January 2025
Available online 3 January 2025

due to inherent system damping. Consequently, any minor disturbances to the structure will gradually dissipate, preventing the onset of sustained oscillations.

Large-amplitude galloping vibrations readily induce mechanical damage to structures. To mitigate this risk, numerous researchers have explored passive control approaches [41–45]. One widely used strategy involves modifying the structure surface. Xing et al. [46] employed surface protrusions on a rectangular bluff body to suppress structural galloping. Their findings demonstrated that both double-sided and all-sided protrusion designs achieved remarkable amplitude suppression ratios. Zhao et al. [47] installed multiple airflow spoilers on power cables of high-speed railways to counteract galloping effects under strong wind conditions. Katsuchi et al. [48] applied spiral protuberances to the stay cables of cable-stayed bridges, effectively reducing the drag force coefficient and mitigating dry galloping. Other surface modifications, such as cables featuring longitudinally parallel protuberances and indentations, have been shown to disrupt shear layer formation, reducing lift on bluff bodies, and diminishing the galloping effect. Additionally, field observations have confirmed that line spacers effectively weaken the power cable galloping [49,50].

Other passive control strategies involve indirect energy dissipation dampers (IED) including tuned mass dampers (TMD) [51,52], tuned liquid dampers (TLD) [53,54], impact dampers (ID) [55,56] and their various hybridizations [57–60]. Furthermore, nonlinear energy sinks (NESs) have garnered considerable attention due to their effectiveness across a broad range of excitations [61–65]. Lou et al. [66] developed a viscoelastic-damping spacer to suppress the iced transmission line galloping. Duan et al. [67] explored the anti-galloping effect of damping droppers on railway contact lines through numerical analysis. Zhang et al. [68] demonstrated that compound damping cables could effectively alleviate the power cable galloping. Dai et al. [69] introduced a novel NES featuring a nonlinear stiffness and linear damping to eliminate galloping, and theoretically analyzed the NES parameter effects on system frequency under coupled conditions and the critical galloping wind speed. Selwanis et al. [70] experimentally validated the galloping suppression capabilities of an NES featuring a freely rotating ball mounted on the top of a bluff body, which also showed potential for suppressing other types of FIVs. Subsequently, a multi-ball configuration was proposed, achieving an enhanced suppression effect [71]. Franzini et al. [72] conceived an NES comprising a mass, a piezoelectric spring, and a linear damper. This design not only suppressed galloping but also facilitated energy harvesting, pioneering a novel approach to passive vibration suppression. NESs function by irreversibly transferring energy from the primary structure to the secondary system [73,74]. However, this approach increases the mass of the original structure, and requires the natural frequency of the secondary system to match the galloping frequency of the primary structure.

To overcome the limitations of passive control strategies, active control technologies are increasingly being researched and developed. Time-delay feedback controllers and their integrations with TMD have been successfully validated for controlling structural galloping [75–77]. However, these applications heavily rely on advanced electronic and control technologies. Furthermore, extensive research has indicated that dynamic behaviors of nonlinear structures subjected to high-frequency excitations can significantly influence their slow response behaviors [78–81], and elevate cut-in wind speeds [82]. Sahoo et al. [83] investigated the effects of parametric and direct high-frequency excitation injection (HFEI) on structural galloping under unsteady winds. Daqaq et al. [84] experimentally demonstrated the effectiveness of HFEI technology by applying high-frequency base excitations near the structure's second modal frequency. This method successfully suppressed the galloping phenomenon and delayed the critical wind speed.

HFEI technology has emerged as a promising method for suppressing galloping. Nevertheless, some challenges hinder its widespread application: (1) effective galloping suppression requires high-frequency excitations with substantial acceleration or force; and (2) the high costs and significant technical challenges of actively applying such excitations remain unavoidable.

This paper introduces an innovative approach that utilizes another form of FIV, namely flutter, to suppress structural galloping. By attaching flags to structures susceptible to galloping, high-frequency periodic flutter is passively triggered by wind flow. This method effectively suppresses galloping before it fully activates, eliminating the need for substantial acceleration or force. The innovations and contributions of this work include: (1) proposal of a novel passive approach for structural galloping suppression using high-frequency flutter; (2) development of a distributed aerodynamic model of the galloping structure that accounts for fluid-solid coupling; (3) analysis of the galloping suppression effect considering factors including external excitation characteristics, wind speed, and position and geometric parameters of flag; (4) exploration of the flag flutter characteristics through wind tunnel tests; (5) validation of the proposed galloping suppression approach under both constant and variable wind conditions. The theoretical galloping model developed in this study is validated by experimental results, guaranteeing the reliability of theoretical analysis. Furthermore, the proposed approach exhibits superior galloping suppression performance across a broad wind speed range, advancing the practicality and feasibility of HFEI technology.

The following contents of this article are organized as follows: Section 2 develops a mathematical model of a classical beam-based galloping system, along with a galloping suppression model incorporating high-frequency flutter excitations. Section 3 examines the galloping suppression effect with high-frequency flutter, including a comprehensive parameter analysis. Section 4 explores the galloping suppression effect under fluctuating and variable wind conditions using the theoretical model. Section 5 presents several experimental studies, including the exploration of flag fluttering dynamics, validation of the galloping model, and verification of the galloping suppression approach under constant and variable wind conditions. Finally, key findings are summarized in Section 6.

2. Galloping suppression approach and modeling

In this section, the galloping suppression approach is introduced firstly, followed by the discussion of its properties and advantages. Subsequently, a mathematical model for galloping suppression is developed based on the Euler-Bernoulli beam theory to reveal the suppression mechanism.

2.1. Galloping suppression approach

An elastically mounted bluff body, as depicted in Fig. 1**(a)**, experiences galloping perpendicular to the flow direction when the wind speed, U, surpasses a critical threshold, resulting in large-amplitude oscillations. The dynamic state of the galloping system can be expressed as

$$M_e\ddot{w}(t) + D_e\dot{w}(t) + K_e w(t) = F_y, \tag{1}$$

where M_e is the mass of the bluff body; D_e denotes the damping coefficient; K_e represents the system stiffness; F_y refers to the aerodynamic force along the y-axis.

In three-dimensional space, a classical galloping system consisting of a cantilever beam with a rectangular bluff body affixed to its free end, is utilized to validate the proposed galloping suppression approach, as illustrated in Fig. 1**(b)**. HFEI technology has been theoretically and experimentally validated to influence slow dynamic responses and suppress galloping in nonlinear systems. However, high-frequency excitations are typically applied actively as base excitations. When the galloping is fully developed with large amplitudes, the required

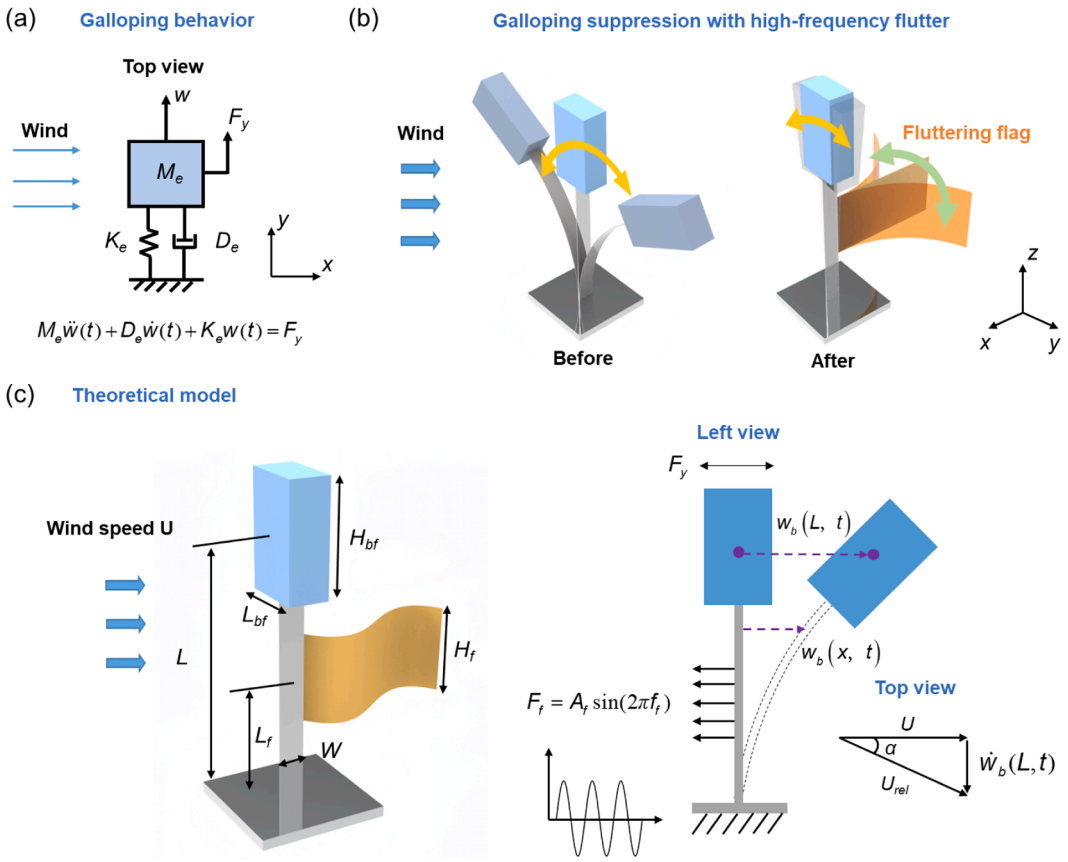

Fig. 1. Proposed galloping suppression approach. (a) Principle of the galloping phenomenon. (b) Schematic representation of the galloping suppression approach with high-frequency flutter. The high-frequency flutter is introduced by attaching a flexible flag. As wind passes through, the rapid flutter of the flag is applied to the system susceptible to galloping, thereby achieving the galloping suppression effect. (c) Aerodynamic modeling of the galloping structure and galloping suppression using high-frequency flutter. The model is established using Euler-Bernoulli beam theory, incorporating the effects of both galloping and fluttering forces.

acceleration for suppression is substantial. These challenges limit the advancement and practical application of HFEI technology in engineering. Herein, a novel galloping suppression approach is proposed in Fig. 1**(b)**, where a flexible flag is fixed between the beam's free and fixed ends. High-frequency excitations are injected into the galloping system through the flag-induced flutter. The novelties and advantages of the proposed approach compared to existing HFEI technologies include: (1) utilizing natural flutter-induced vibrations instead of actively injecting external high-frequency excitations; (2) suppressing galloping before it is fully activated, owing to the rapid initiation of high-frequency flutter; (3) requiring small force amplitudes and simplifying implementation challenges by generating surface load excitations rather than point load excitations; (4) greater flexibility in excitation positioning, allowing placement anywhere between the fixed and free ends of the cantilever beam.

2.2. Aerodynamic model

According to the Euler-Bernoulli beam theory, the dynamic behavior of the main beam undergoing galloping (see Fig. 1**(c)**) can be governed by

$$E_b I_b \frac{\partial^4 w_b(x,t)}{\partial x^4} + C_a \frac{\partial w_b(x,t)}{\partial t} + C_s I_b \frac{\partial^5 w_b(x,t)}{\partial x^4 \partial t} + m\frac{\partial^2 w_b(x,t)}{\partial t^2} = F_y \delta(x-L) + F_{ft}, \tag{2}$$

where E_b and I_b are Young's modulus and the moment of inertia of the cantilever beam; $w_b(x,\ t)$ refers to the transverse displacement of the beam; C_a and C_s denote strain and viscous air damping coefficients, respectively; m represents the distributed beam mass.

According to the quasi-steady hypothesis, the transverse galloping force can be represented as

$$F_y = \frac{1}{2}\rho H_{bf} L_{bf} U^2 \sum_{i=1}^{3} A_i \alpha^i, \alpha = \frac{\dot{w}_b(L,t)}{U} + w'_b(L,t), \tag{3}$$

where ρ refers to the air density; H_{bf} and L_{bf} represent the height and length of bluff body; A_i denote the aerodynamic coefficients. The approach to determining aerodynamic coefficients A_i may be found in [85]. Herein, A_1, A_2, and A_3 are determined as 2.7, 0 and −11.5, respectively, based on static wind tunnel tests. α is the attack angle, and $w'_b(L,t)$ is the beam rotation angle.

When the flexible flag flutters, its fixed end transmits a transverse surface load to the beam. In a two-dimensional model, the surface load degenerates into a line load, applied uniformly and discretely along the beam, in units of N. The total fluttering force is represented as

$$F_{ft} = \sum_{j=1}^{n+1} A_f \sin\left(2\pi f_f t\right) \delta\left[x - L_s + \frac{H_f}{n}(j-1)\right], \tag{4}$$

where L_f refers to the distance between the flag center and the base; L_s is the distance between the bottom of the flag and the base, and $L_s = L_f - \frac{H_f}{2}$; H_f is the flag height; n is the interval between discrete flag loads. Flutter is treated as an external force because the focus is on its high-frequency characteristics rather than its other unique properties. The flag's flutter can be approximated to be a periodic motion with a

specific frequency [86], typically ranging from a few to hundreds of Hertz. To reveal common mechanisms and offer insights into the optimal galloping suppression design, the fluttering force is simplified as a sinusoidal excitation with two independent variables: amplitude A_f and frequency f_f, and is uniformly applied over the interval $[L_f - \frac{H_f}{2}, L_f + \frac{H_f}{2}]$.

The beam deflection in the modal coordinate relative to position x and time t can be expressed as

$$w_b(x,t) = \sum_{r=1}^{\infty} \varphi_r(x)\eta_r(t), \tag{5}$$

where $\varphi_r(x)$ represents the mass-normalized mode shapes of the rth mode under undamped free vibration, and $\eta_r(t)$ refers to the modal coordinate.

The process of solving mass-normalized modes $\varphi_r(x)$ can refer to Appendix A, and the undamped modal frequency ω_r can be expressed as

$$\omega_r = \lambda_r^2 \sqrt{\frac{E_b I_b}{mL^4}}. \tag{6}$$

Thus, the governing equations in the modal coordinate system can be rewritten as

$$\ddot{\eta}_r(t) + 2\zeta_r\omega_r\dot{\eta}_r(t) + \omega_r^2\eta_r(t) = f_y + f_{fr}, \tag{7}$$

where ζ_r denotes the modal damping ratio; f_{yr} and f_{fr} are the galloping force and the total fluttering force in the modal coordinate, and are given as

$$f_{yr} = \varphi_r(L) \times \frac{1}{2}\rho H_{bf} L_{bf} U^2 \sum_{i=1}^{3} A_i \left[\frac{\sum_{r=1}^{\infty} \varphi_r(L)\dot{\eta}_r(t)}{U} + \sum_{r=1}^{\infty} \varphi'_r(L)\eta_r(t) \right]^i, \tag{8}$$

$$f_{fr} = A_f \sin\left(2\pi f_f t\right) \sum_{j=1}^{n+1} \varphi_r\left[x - L_s + \frac{H_f}{n}(j-1)\right]. \tag{9}$$

The first six modes are considered to investigate the potential galloping suppression effect, and a state vector is introduced

$$\boldsymbol{X} = \begin{bmatrix} X_1 \\ X_2 \\ \vdots \\ X_{2r-1} \\ X_{2r} \end{bmatrix} = \begin{bmatrix} \eta_1(t) \\ \dot{\eta}_1(t) \\ \vdots \\ \eta_r(t) \\ \dot{\eta}_r(t) \end{bmatrix} \quad r = 1, 2 \ldots 6. \tag{10}$$

The governing equations in the state space can be expressed as

$$\dot{\boldsymbol{X}} = \begin{bmatrix} \dot{\eta}_1(t) \\ \ddot{\eta}_1(t) \\ \vdots \\ \dot{\eta}_r(t) \\ \ddot{\eta}_r(t) \end{bmatrix} = \begin{bmatrix} X_2 \\ -2\zeta_1\omega_1 X_2 - \omega_1^2 X_1 + f_{f1} + f_{y1} \\ \vdots \\ X_{2r} \\ -2\zeta_r\omega_r X_{2r} - \omega_r^2 X_{2r-1} + f_{fr} + f_{yr} \end{bmatrix}. \tag{11}$$

By solving the state-space equations, the transverse displacement of the beam $w_b(x, t)$ can be obtained from Eq. (5) to evaluate the galloping suppression performance. It is important to note that certain assumptions and limitations exist within the theoretical modeling process. First, the use of a low-order fitting function for the galloping force expression simplifies calculations but may introduce minor prediction errors in the system's galloping characteristics. Second, the fluttering force is modeled as a single-frequency excitation and is assumed to be uniformly distributed because it is difficult to measure accurately, which may cause discrepancies between predicted and actual galloping suppression effects. Therefore, the subsequent theoretical analysis mainly aims to prove the effectiveness of high-frequency excitation in suppressing galloping. The actual suppression effect would be affected by other potential overlooked factors induced by fluid-solid couplings.

3. Parameter analysis

This section presents a detailed analysis of the galloping suppression using the developed aerodynamic model. Firstly, the galloping suppression mechanism is investigated under varying fluttering frequency and amplitude conditions, revealing two characteristic frequencies for galloping suppression. Subsequently, the effects of wind speed, flag position and flag parameter on galloping suppression are explored. These findings highlight galloping suppression mechanisms and rules, offering valuable insights into the optimal design of fluttering flags.

3.1. Galloping suppression mechanism analysis

To reveal the galloping suppression mechanism using high-frequency flutter, Fig. 2**(a), (b)** and **(c)** present the normalized amplitude against fluttering frequency and force amplitude at wind speeds of 3, 6, and 10 m/s, respectively. The structural parameters used in the theoretical analysis are listed in Appendix B. The normalized galloping amplitude A_u is defined as A/L, where A is the galloping amplitude and L is the cantilever beam length. To exclude resonant effects, the two-dimensional views limit the maximum amplitude to situations without high-frequency excitation. Herein, the force is presented as a line load, in units of N/m. A characteristic frequency f_{c2} of 45 Hz, proximate to the second modal frequency, is identified as the optimal frequency to activate the galloping suppression with minimal force amplitude. This finding aligns with results reported in the literature [84]. Notably, the critical force value remains relatively constant at varying wind speeds. However, the fluttering force amplitude required at 45 Hz is stringent, and excessive amplitudes may induce resonance at the second modal frequency f_{r2} of 41.09 Hz. Another notable observation occurs near the third modal frequency f_{r3}, where the characteristic frequency f_{c3} of 124 Hz is also effective at initiating galloping suppression. In this case, the critical force value increases with wind speed. Furthermore, when the excitation frequency lies between the first and second modal frequencies, galloping suppression remains achievable but requires a higher force amplitude. Meanwhile, the lower critical force increases as wind speed rises. To demonstrate that the characteristic frequencies f_{c2} and f_{c3} are closely related to the second and third modal frequencies f_{r2} and f_{r3} of the system, additional material is provided in Appendix C. Additionally, the relationship between the galloping suppression effect and system galloping force is explored.

3.2. Effect of wind speed

Given the distinctive galloping suppression phenomena observed near the second and third modal frequencies, the critical conditions for initiating suppression under both situations have been investigated at varying wind speeds. As illustrated in Fig. 3**(a)**, with the introduction of a 45 Hz high-frequency excitation, the lower critical force for galloping suppression gradually increases with wind speed. Conversely, the upper critical force decreases as wind speed increases, narrowing the suppression bandwidth due to the increased likelihood of triggering resonant effects at the second modal frequency. As shown in Fig. 3**(b)**, when a 124 Hz high-frequency excitation is applied, the lower critical force for galloping suppression rises significantly with wind speed, tripling from 10 N/m to 30 N/m as the wind speed increases from 3 m/s to 10 m/s. Within a force amplitude range of up to 100 N/m, no upper critical limit is observed, and the suppression is maintained as long as the force amplitude exceeds the lower critical force. If high-frequency excitations are applied actively, galloping suppression can be achieved across a broad range of wind speed at minimum cost by maintaining the excitation frequency at 45 Hz. It is important to note that this analysis

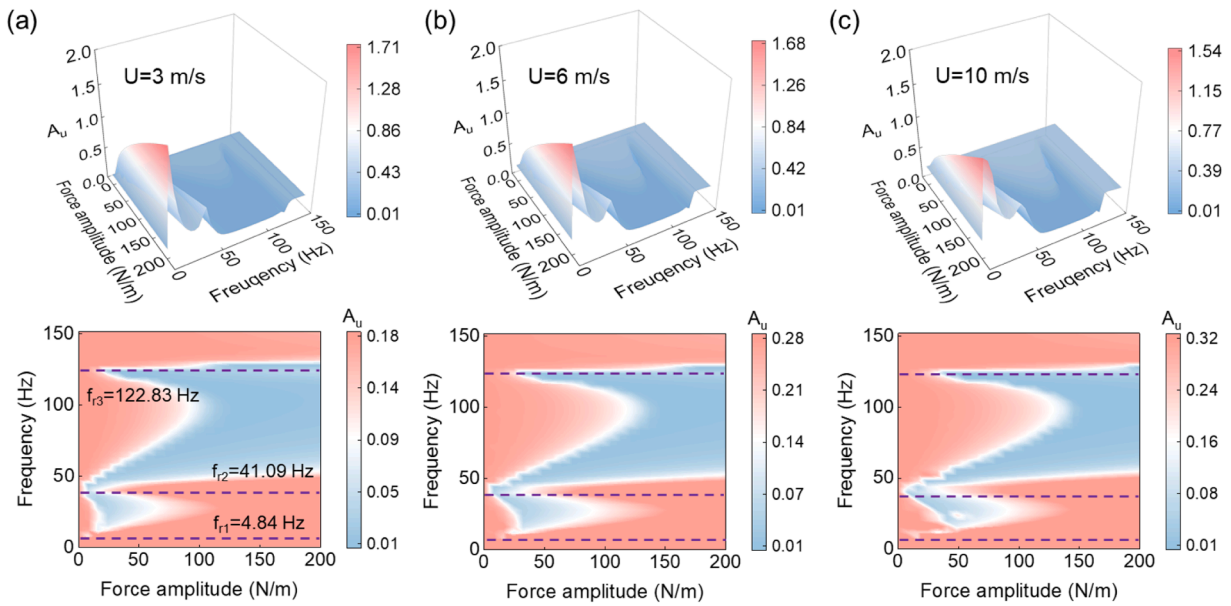

Fig. 2. Galloping suppression mechanism analysis. (a) Three-dimensional and their two-dimensional views of galloping amplitude versus flag fluttering frequency and force amplitude and its two-dimensional view at wind speeds of 3 m/s, (b) 6 m/s and (c) 10 m/s. All two-dimensional views limit the maximum amplitude to situations without high-frequency excitation to exclude resonant effects. The purple dashed lines indicate the first three modal frequencies of the system.

assumes constant wind speeds, and does not account for potential fluctuations.

3.3. Effect of flag position

To explore the impact of load position on galloping suppression, the normalized flag position P_u is defined as L_f/L. As depicted in Fig. 3**(c)**, under a 45 Hz high-frequency excitation, positioning the flag closer to the middle of the beam results in a lower critical force for galloping suppression. However, this arrangement also leads to a more rapid attenuation of the galloping suppression as the force amplitude increases. As shown in Fig. 3**(d)**, when the excitation at a frequency of 124 Hz is injected, the lower critical force increases as the flag position approaches the midpoint of the beam. When the flag is positioned near the middle of the beam ($0.5 \leq P_u \leq 0.6$), activating the galloping suppression effect becomes more challenging. Nonetheless, the most effective suppression is observed when the flag is positioned close to the midpoint, despite a slight increase in the lower critical force.

3.4. Effect of flag parameter

The flag fluttering behavior in a uniform wind is intricately related to its non-dimensional bending stiffness and mass ratio [86]. They can be expressed as

$$K_b = \frac{E_f {T_f}^3}{12(1-\nu^2)\rho_f U^2 L_f^3}, \tag{12}$$

$$M^* = \frac{\rho_f T_f}{\rho_a L_f}, \tag{13}$$

where E_f is Young's modulus of the flag; T_f refers to the flag thickness; ν is the Poisson's ratio; ρ_a and ρ_f represent air and flag material densities; L_f is the flag length.

Changes in the flag's length and thickness affect the mass ratio, which in turn influences the fluttering frequency. To ensure consistency in the investigation of the galloping suppression effect under constant-frequency excitations, the flag length and thickness are maintained constant. Only the width is varied, under the assumption that the width variation does not affect the fluttering frequency. Additionally, as the flag serves as an additional surface load (line load in the two-dimensional model) on the galloping structure, increasing the flag width enhances both the loading surface and total fluttering force. The normalized width is defined as $W_{fu}=H_f/L$. As shown in Fig. 3**(e)**, the lower critical force decreases with an increased flag width when an excitation frequency near f_{r2} is applied, indicating a more readily triggered galloping suppression with an enlarged loading surface. However, this requires stringent control over the force amplitude to avoid weakening the suppression effect. As shown in Fig. 3**(f)**, when a 124 Hz high-frequency excitation is injected, the lower critical force for triggering galloping suppression also decreases as the flag width increases. Overall, adjusting the flag width is an effective method to modulate the fluttering force, but the benefits gradually diminish when the normalized width W_{fu} exceeds 0.3.

4. Galloping suppression under dynamic wind conditions

In the foregoing analysis, wind speed is considered to be constant. However, in natural environments, wind speed is rarely constant, with fluctuations being a common occurrence, which makes galloping suppression more challenging [83]. To address this, Sections 4.1 and 4.2 investigate the galloping suppression performance of proposed approach under wind conditions with small fluctuations and large variations, respectively, to demonstrate its effectiveness in natural environments.

4.1. Galloping suppression under fluctuating wind conditions

Here, the fluctuating wind is expressed as

$$U = U_0 + A_e U_0 \sin(2\pi f_e t), \tag{14}$$

where U_0 is the base wind speed; A_e and f_e denote the amplitude fluctuating coefficient and fluctuating frequency of wind speed.

Given that the minimum fluttering force required increases with wind speed and is relatively high with an excitation at f_{c3}, this analysis focuses on the galloping suppression performance with an excitation at f_{c2} under fluctuating wind speeds. As shown in Fig. 4**(a)-(d)**, assuming a low-frequency wind speed disturbance of 1 Hz, fluctuations in the galloping amplitude are observed when $A_e \geq 0.1$. After suppression, the

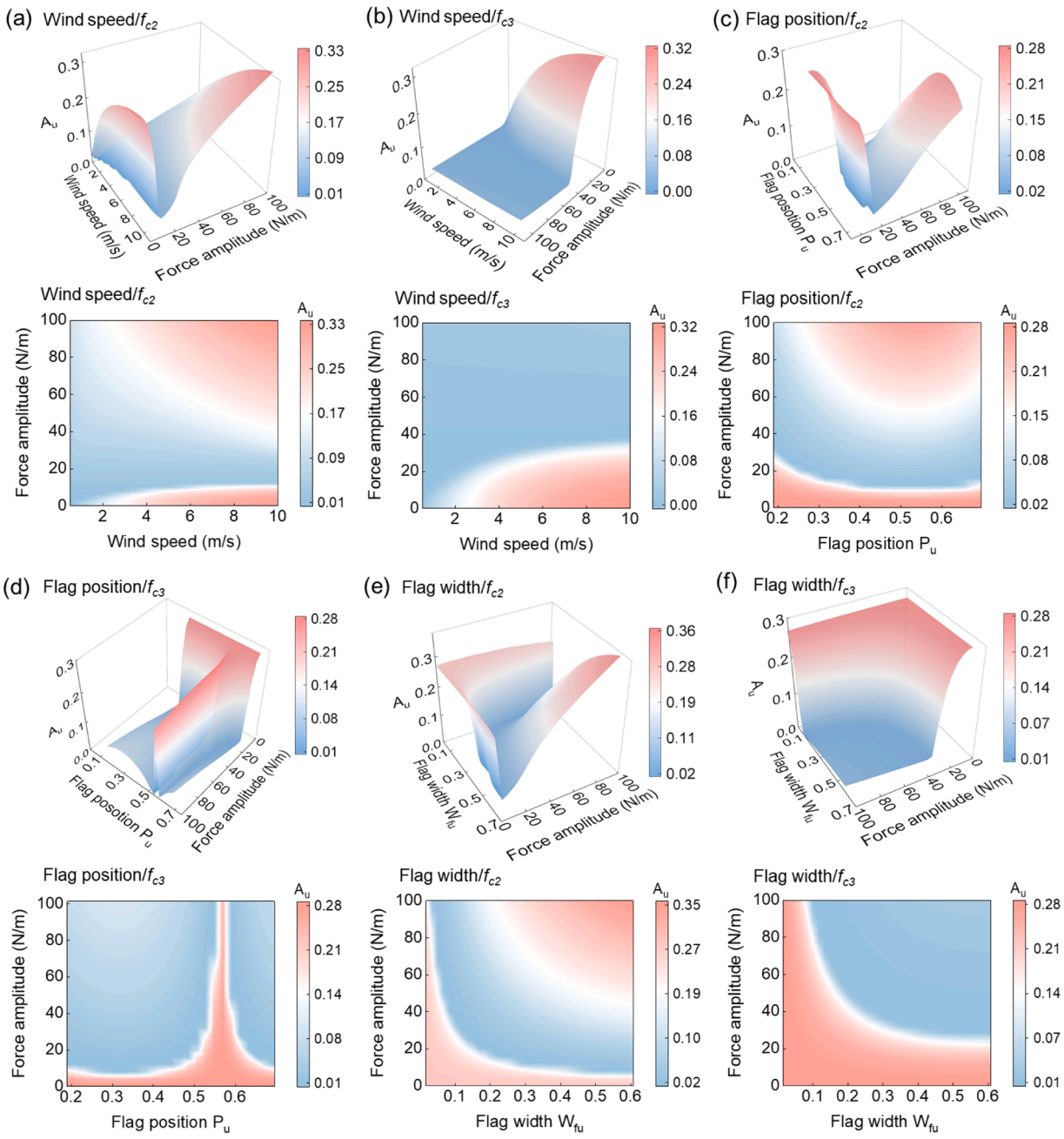

Fig. 3. Parameter analysis of galloping suppression. (a) Three-dimensional and their two-dimensional views of galloping amplitude versus wind speed and force amplitude with excitations at 45 Hz and (b) 124 Hz. (c) Three-dimensional and their two-dimensional views of galloping amplitude versus flag position and force amplitude with excitations at 45 Hz and (d) 124 Hz at 6 m/s. (e) Three-dimensional and their two-dimensional views of galloping amplitude versus flag width and force amplitude with excitations at 45 Hz and (f) 124 Hz at 6 m/s.

amplitude decreases to 0.03, approximately 1/10 of its original value, and remains relatively stable despite variations in A_e. Subsequently, when the fluctuating frequency f_e is increased to 25 Hz and 50 Hz (see Fig. 4**(e)** and **(f)**), the impact of wind speed fluctuations on the original galloping amplitude becomes small. However, when f_e=50 Hz, the suppressed amplitude exhibits fluctuations corresponding to the galloping frequency, although no significant increase in amplitude is observed. This is primarily attributed to high-frequency wind speed fluctuations partially offsetting the suppression effect of the injected high-frequency excitation.

4.2. *Galloping suppression under variable wind conditions*

To further assess the efficacy of the proposed galloping suppression approach under variable wind conditions, the wind speed is varied with a change rate of 1 m/s^2, as depicted in Fig. 4**(g)** and **(h)**. The suppressed amplitude stabilizes at 2 s and 2.2 s under increasing and decreasing wind conditions, respectively, and remains stable despite further variations in wind speed. When the change rates are increased to 5 m/s^2 and 10 m/s^2, galloping continues to be effectively suppressed with the injection of high-frequency excitation, as illustrated in Fig. 4**(i)**-**(m)**. These results confirm the robustness of high-frequency flutter in mitigating structural galloping under dynamic wind conditions. Although high-

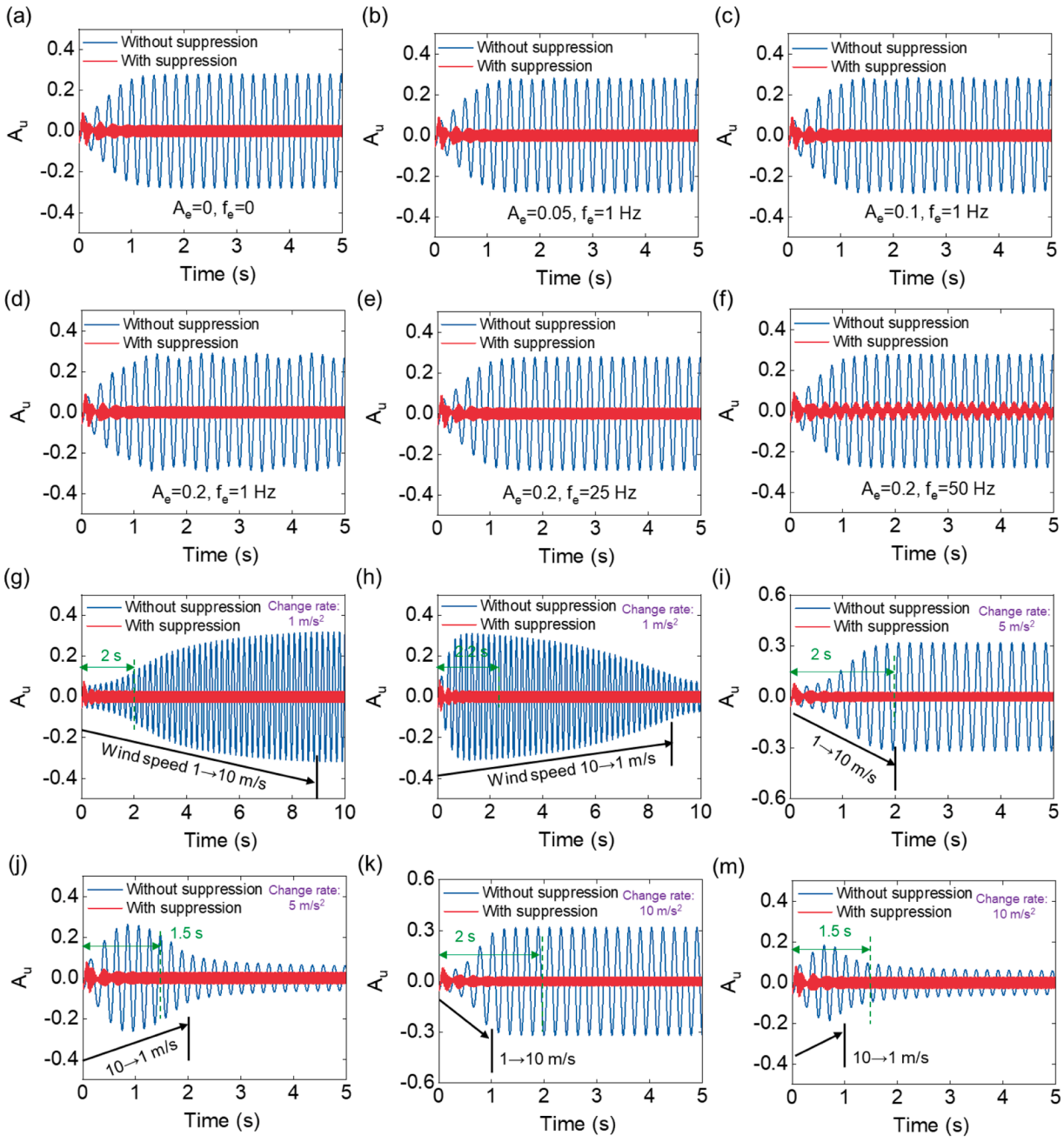

Fig. 4. Galloping suppression analysis under dynamic wind conditions. (a) Galloping suppression under fluctuating wind conditions when A_e=0, f_e=0; (b) A_e=0.05, f_e=1 Hz; (c) A_e=0.1, f_e=1 Hz; (d) A_e=0.2, f_e=1 Hz; (e) A_e=0.2, f_e=25 Hz; and (f) A_e=0.2, f_e=50 Hz. The base wind speed is 6 m/s, and A_e and f_e refer to the amplitude and frequency of wind fluctuations. (g) Galloping suppression under variable wind conditions at increased and (h) decreased wind speed with a change rate of 1 m/s^2. (i) Galloping suppression at increased and (j) decreased wind speed with a change rate of 5 m/s^2. (k) Galloping suppression at increased and (m) decreased wind speed with a change rate of 10 m/s^2. The frequency and force amplitude of the injected excitation is 45 Hz and 10 N/m, respectively.

frequency excitations can be artificially implemented to achieve galloping suppression as shown in Fig. 4, the real-world application of high-frequency flutter using a flexible flag will require some time for full activation. However, this activation occurs significantly faster than the onset of galloping. Furthermore, the fluttering frequency and force of the flag will vary with fluctuating and variable wind conditions, necessitating the re-establishment of a new equilibrium. These factors are not accounted for in the theoretical model. Therefore, to corroborate the effectiveness of flag-induced flutter in suppressing galloping, further experimental investigations will be conducted in the subsequent section.

5. Experimental validation

This section presents several experimental investigations and validations to support the proposed galloping suppression scheme and previous theoretical analysis. Section 5.1 introduces the experimental setup of the wind tunnel. Section 5.2 validates the distributed galloping model using experimental data. Section 5.3 explores the flag flutter characteristics for the optimal galloping suppression design. Sections 5.4 and 5.5 experimentally validate the galloping suppression performance under constant and variable winds, respectively.

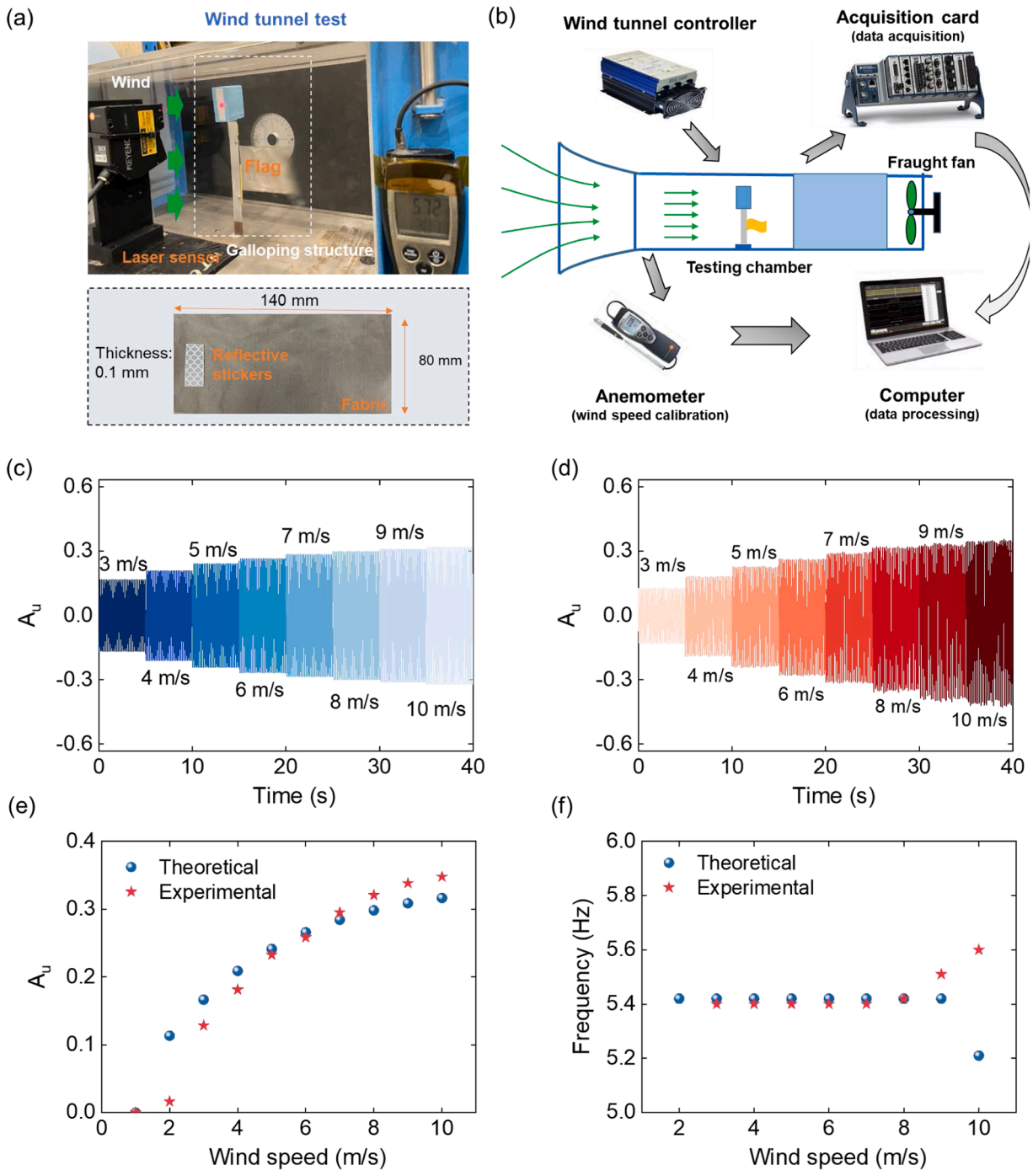

Fig. 5. Experimental setup and theoretical galloping model validation. (a) Photograph of the experimental validation of the proposed galloping suppression approach using flexible flag. Reflective stickers are attached to the surfaces of the bluff body and the flexible flag for displacement measurement. (b) Experimental setup and data acquisition process. An anemometer and a laser sensor are employed for wind speed calibration and displacement measurement. The sensor signals are acquired by a data acquisition device and displayed on a laptop. (c) Theoretical and (d) experimental galloping amplitudes in the time domain. (e) Comparisons of theoretical and experimental results in galloping amplitude and (f) frequency over a wind speed range of 3–10 m/s at an interval of 1 m/s.

5.1. Experimental setup for wind tunnel tests

The experimental validation for the proposed galloping suppression approach is conducted using a wind tunnel (featuring a cross-section of 300 × 300 mm^2) in the CEE Protective Engineering Lab of Nanyang Technological University, as depicted in Fig. 5**(a)**. The galloping structure consists of an aluminum beam with a thickness of 0.6 mm, and a foam bluff body with a size of 50 × 30 × 60 mm^3. The flexible flag is made of Ni-coated fabric and has a size of 140 × 0.1 × 80 mm^3. Reflective stickers are attached to the surfaces of the bluff body and the flexible flag for displacement measurement. Fig. 5**(b)** presents the experimental setup and data acquisition process. An anemometer (TESTO 425) is employed to calibrate the wind speed during the test. The displacements of both the galloping structure and flexible flag are measured using a laser sensor (Keyence LK-H157). The sensor signals are captured by an NI 9229 DAQ module, and subsequently processed with a

portable computer. During the test, wind speed ranges from 1 m/s to 10 m/s, corresponding to a Reynolds number R_e ranging from 21,500 to 215,000.

5.2. Theoretical model validation

The distributed galloping model serves as the primary framework in aerodynamic modeling, and its effectiveness is crucial for reliable theoretical analysis. Fig. 5**(c)** and **(d)** illustrate both theoretical and experimental displacements of the free end of the cantilever beam undergoing galloping in the time domain, while the corresponding displacement amplitude and dominant frequency are summarized in Fig. 5**(e)** and **(f)**. Theoretically, structural galloping can be initiated at the wind speed of 2 m/s; however, it is fully triggered at 3 m/s in experimental tests. The experimental displacements demonstrate good consistency with the theoretical calculations. The discrepancies observed at low and high wind speeds are primarily due to the inability of the theoretical model to accurately represent the galloping forces. From the perspective of the galloping frequency, the model's accuracy is further validated. As wind speed increases, the theoretical galloping frequency exhibits a slight decrease, aligning with the results reported in reference [87]. Conversely, the experimental frequency slightly increases at high-speed winds, likely due to large-amplitude galloping oscillations being affected by the surrounding flow field in a wind tunnel chamber that is not sufficiently large.

5.3. Flag dynamic characteristics

The flag dynamic characteristics are measured using a laser sensor with a reflective sticker attached near the flag's fixed end, as shown in Fig. 6**(a)**. During displacement measurements, the bluff body at the top of the cantilever beam is removed, allowing the beam to behave as a relatively rigid support in the wind. The measured flag displacement in the time and frequency domains at the wind speed of 5 m/s are illustrated in Fig. 6**(b)** and **(c)**. Based on the above analysis, the critical fluttering wind speed and fluttering frequency are critical for galloping suppression. Therefore, the flag dynamic characteristics are experimentally investigated with the length varying from 80 mm to 140 mm and the aspect ratio varying from 1.75 to 3, while maintaining a constant thickness. As shown in Fig. 6**(d)**, increasing the flag length and aspect ratio reduces the critical fluttering wind speed, broadening the potential for galloping suppression across a broader wind speed range. In

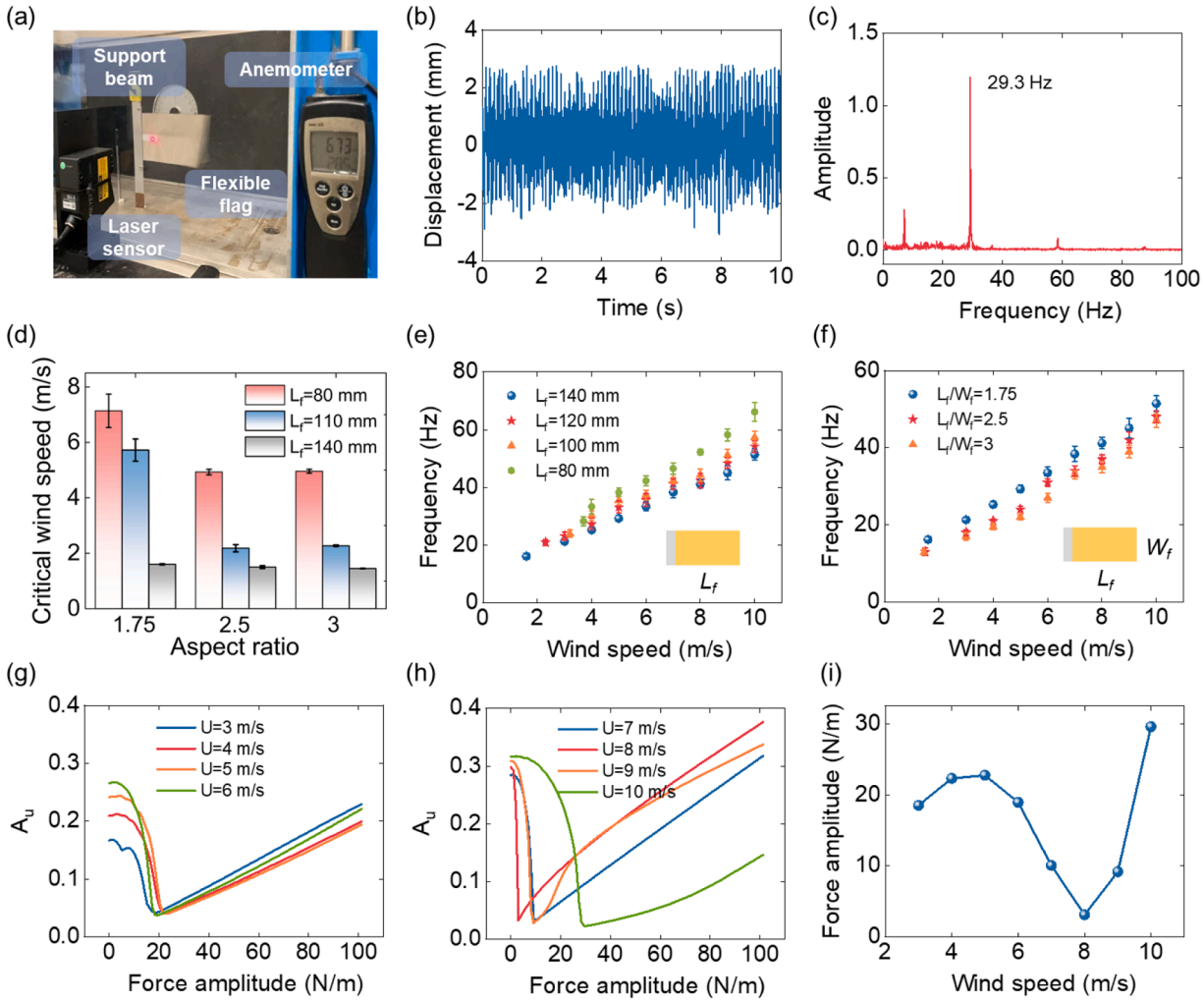

Fig. 6. Flag dynamic characteristics. (a) Experimental setup for flag fluttering dynamics tests. (b) Displacement of the flag near its fixed end at 5 m/s and (c) its frequency domain characteristics. (d) Critical fluttering wind speed versus flag length and flag aspect ratio. (e) Flag fluttering frequency versus wind speed and flag length with a constant aspect ratio of 1.75. (f) Flag fluttering frequency versus wind speed and aspect ratio with a constant length of 140 mm. (g) Suppressed amplitudes versus force amplitude over a wind speed range of 3 m/s–6 m/s and (h) 7 m/s–10 m/s. These results are calculated using theoretical model with a flag length of 140 mm. (i) Optimal fluttering force values at different wind speeds.

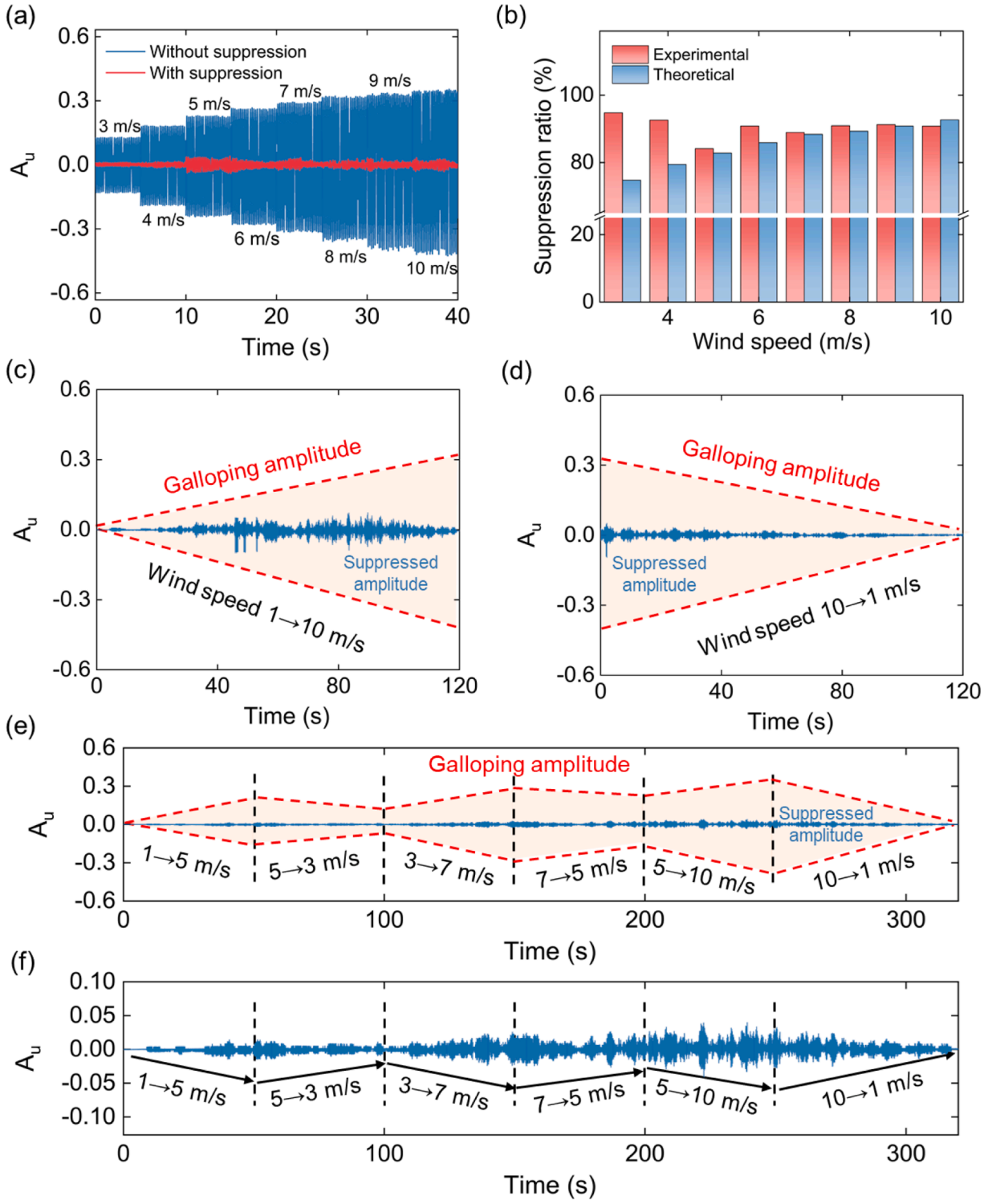

Fig. 7. Galloping suppression experiments under constant and variable wind conditions. (a) Comparison of experimental amplitude with/without flutter suppression. (b) Comparison of theoretically and experimentally optimal suppression ratios over a wind speeds range of 3 m/s–10 m/s at an interval of 1 m/s. (c) Suppressed galloping amplitude under variable wind conditions with wind speed increasing from 1 m/s to 10 m/s. (d) Suppressed galloping amplitude under variable wind conditions with wind speed decreasing from 10 m/s to 1 m/s. (e) Suppressed amplitude under reciprocally variable wind conditions and (f) its detailed view. The red dashed line represents the galloping amplitude without suppression.

addition, as shown in Fig. 6**(e),** the flag fluttering frequency increases approximately linearly with wind speed, aligning with experimental findings reported in relevant literature [88–90]. Notably, a longer flag corresponds to a lower fluttering frequency due to the decreased mass ratio [89]. Aspect ratio variations also affect the fluttering frequency. As illustrated in Fig. 6**(f)**, a larger aspect ratio reduces the fluttering frequency to some extent. Given the variation of flag fluttering frequency with wind speed, meticulous attention to its frequency characteristics across the entire operational wind speed range is necessary. Since the second modal frequency is 41.09 Hz, maintaining the flag fluttering frequency near this value is advantageous for triggering galloping suppression. Moreover, it is critical to ensure that the maximum flag fluttering frequency does not substantially exceed 41.09 Hz, as higher frequencies necessitate larger fluttering forces at high wind speeds, as demonstrated in Fig. 2. Ultimately, the flag length is determined to be 140 mm, yielding a fluttering frequency range of 16.2 Hz–51.7 Hz across the operational wind speed range.

Prior experimental tests have demonstrated effective galloping suppression when the flag dimensions are 140 × 80 mm^2 (L_f/W_f=1.75). Based on the fluttering frequency of this flag, the relationship between the galloping suppression performance and fluttering force at different wind speeds is first analyzed, as shown in Fig. 6**(g)** and **(h)**. For wind speeds ranging from 3 m/s to 6 m/s, the minimum suppressed amplitude A_u consistently remains around 0.05, with a relatively stable optimal fluttering force for galloping suppression. However, as wind speed increases to 7 m/s–10 m/s, variations in flag fluttering frequency significantly influence the suppressed amplitude curve, with the optimal fluttering force initially decreasing and then increasing. The optimal fluttering forces across different wind speeds are summarized in Fig. 6 **(i)**. It is observed that galloping suppression is more readily triggered with minimal fluttering force at wind speeds of 7 m/s–9 m/s, because the flag fluttering frequency closely approximates the second modal frequency of the system. Outside this range, a larger fluttering force is required for effective suppression.

Accurately capturing and measuring the fluttering force applied to the beam presents significant challenges due to the following reasons: (1) the narrow space between the beam and the flag, along with the surface contact between them, create substantial obstacles for sensor installation and surface force measurement; (2) the fluttering force is typically weak and difficult to capture accurately; (3) the beam itself undergoes weak vibrations in the wind, which significantly interferes with the measurement of the fluttering force applied to it. However, as indicated in Fig. 3**(e)**, increasing the flag width results in a larger total reaction force applied to the beam and an enhanced galloping suppression, which can serve as an indirect tuning approach. The specific experimental results regarding the galloping suppression performance will be detailed in the next section.

5.4. Galloping suppression at constant winds

Firstly, the galloping suppression performance with high-frequency flutter is validated under constant wind conditions, as shown in Fig. 7 **(a)**. In the time domain, the normalized amplitude A_u is significantly suppressed across the wind speed range of 3 m/s–10 m/s. Notably, the suppressed amplitude is relatively low even at high wind speeds of 7 m/s–9 m/s, confirming the theoretical predictions that a superior galloping suppression effect can be achieved with minimal fluttering force, as demonstrated in Fig. 6**(i)**. However, the galloping suppression effect at 5 m/s is suboptimal, due to the relatively large required fluttering force and the actual fluttering force possibly not reaching the optimal value yet.

In Fig. 7**(b)**, the optimal suppression ratios calculated using the theoretical model are compared with those achieved in experimental tests. The feasibility of galloping suppression with high-frequency flutter is demonstrated from both theoretical and experimental perspectives. It is noted that this does not constitute a direct validation of the galloping supression model, as the fluttering force is difficult to measure directly, as previously mentioned. Nonetheless, the fluttering frequency and all other parameters used in the model are consistent with the test values and experimental configuration. It is observed that the galloping suppression achieved in the experiments is more pronounced at wind speeds of 3 m/s and 4 m/s. When the wind speed exceeds 4 m/s, the theoretical and experimental suppression ratios exhibit good consistency. The differences observed at low wind speeds may be attributed to the following reasons: (1) the installation method or overlooked resistance may make the onset of the galloping more difficult, facilitating galloping suppression more readily than in ideal situations; (2) the theoretical model may not fully account for certain aspects of fluid-solid coupling under actual conditions. Overall, the experimental results demonstrate galloping suppression ratios of 85–95% over the constant wind speed interval of 3 m/s–10 m/s.

5.5. Galloping suppression at variable winds

To validate the proposed approach under fluctuating wind conditions, galloping suppression performance is tested at wind speeds varying from 1 m/s to 10 m/s over 120 s. As shown in Fig. 7**(c)** and **(d)**, a significant reduction in amplitude is observed after suppression, under both increasing and decreasing wind speed conditions. Unlike under constant wind speed conditions, transient peaks appear in the suppressed displacement due to sustained changes in wind speed. Concurrently, the flag's fluttering state is dynamically updated to establish a new equilibrium. Additionally, a more effective suppression is achieved under the decreasing wind speed condition because of the hysteresis phenomenon of the flag [91]. As wind speed decreases, the flag's fluttering frequency decreases more gradually than ideally expected, deviating more slowly from the second modal frequency, thereby enhancing the galloping suppression. To simulate natural wind fluctuations more realistically, the wind speed is tuned reciprocally with a slower change rate. As illustrated in Fig. 7**(e)** and **(f)**, the suppressed amplitude appears relatively smoother at a lower wind speed change rate, with at least 85% of the amplitude suppressed throughout the entire testing process. A visual demonstration of galloping suppression under reciprocally variable wind speed is supplemented in **Movie S1**. These results demonstrate that the proposed approach shows great promise for engineering and natural scenarios.

6. Conclusions

This paper proposes and implements a novel passive galloping suppression approach that leverages high-frequency flutter, addressing the challenges of actively applying HFEI technology in engineering. By introducing a meticulously designed flag to the structure, galloping is preemptively suppressed through flag flutter before it fully develops, eliminating the need for excessive excitation force or acceleration. Numerical analysis and experimental results validate its superiority of suppressing galloping over a broad range of wind speeds.

To elucidate the galloping suppression mechanism using high-frequency flutter, an aerodynamic model has been developed, followed by comprehensive parameter analysis. A characteristic frequency, f_{c2}, near the second modal frequency, initiates galloping suppression with minimal fluttering force, maintaining a relatively constant critical force across varying wind speeds. However, the force amplitude must be carefully regulated to avoid resonance. Another characteristic frequency, f_{c3}, close to the third modal frequency, also triggers galloping suppression with low fluttering force, although the critical force

increases with wind speed. Notably, sustained suppression requires the fluttering force to exceed a specific lower critical value for each wind speed. The positioning of the flag also plays a pivotal role in optimizing suppression. For fluttering excitation at f_{c2}, positioning the flag close to the beam's midpoint facilitates suppression initiation. Conversely, for excitation at f_{c3}, the flag should be placed away from the midpoint to ensure effective suppression. Additionally, increasing the flag width enhances the suppression for both situations by amplifying the total fluttering force, though the improvement diminishes as the width continues to increase.

Furthermore, experimental investigations into flag dynamics offer insights into the optimal galloping suppression design. Results show that the dominant fluttering frequency increases approximately linearly with wind speed. A longer flag lowers the dominant frequency, extending the operational wind speed range and broadening the suppression spectrum. Ideally, the fluttering frequency range of the flag should align with f_{c2} to minimize the galloping suppression threshold, while ensuring the maximum fluttering frequency does not significantly exceed f_{c2}, to maintain achievable force requirements.

Finally, validation tests demonstrate that the optimized flag yields the required high-frequency flutter, reducing galloping amplitudes by 85–95 % across constant wind speeds ranging from 3 m/s to 10 m/s. The method also adapts effectively to variable wind speed conditions, showcasing its suitability for natural wind environments.

In conclusion, this approach alters conventional HFEI technology from an active to a passive modality, simplifying implementation and saving financial costs. Beyond their decorative role, flags on engineering structures effectively suppress galloping, highlighting their potential for diverse applications.

CRediT authorship contribution statement

Liwei Dong: Writing – review & editing, Writing – original draft, Validation, Software, Methodology, Funding acquisition, Data curation. **Chaoyang Zhao:** Writing – review & editing, Validation, Software, Methodology, Data curation. **Shuai Qu:** Resources, Formal analysis, Data curation. **Wei Ding:** Writing – review & editing, Resources, Formal analysis. **Guobiao Hu:** Supervision, Resources, Investigation. **Chengjia Han:** Writing – review & editing, Software, Resources, Conceptualization. **Yaowen Yang:** Writing – review & editing, Project administration, Funding acquisition, Formal analysis, Conceptualization.

Declaration of competing interest

The authors declare that they have no known competing financial interests or personal relationships that could have appeared to influence the work reported in this paper.

Acknowledgment

This work was sponsored by the NTU grant 020671–00001 and China Scholarship Council (Grant No. 202206260157).

Supplementary materials

Supplementary material associated with this article can be found, in the online version, at doi:10.1016/j.ijmecsci.2025.109928.

Appendix A. Mass-normalized mode shapes under boundary conditions

Considering all boundary conditions, the mass-normalized mode shapes $\varphi_r(x)$ can be written as [92]

$$\varphi_r(x) = C_r\left[\cos\frac{\lambda_r}{L}x - \cosh\frac{\lambda_r}{L}x + \beta_r\left(\sin\frac{\lambda_r}{L}x - \sinh\frac{\lambda_r}{L}x\right)\right], \tag{A1}$$

where

$$\beta_r = \frac{mL(\sin\lambda_r - \sinh\lambda_r) + \lambda_r M_{bf}(\cos\lambda_r - \cosh\lambda_r)}{mL(\cos\lambda_r + \cosh\lambda_r) - \lambda_r M_{bf}(\sin\lambda_r - \sinh\lambda_r)}. \tag{A2}$$

The eigenvalues λ_r in Eq. (A2) are given by solving the following characteristic equation

$$\begin{aligned} &1 + \cos\lambda\cos\lambda + \frac{\lambda M_{bf}}{mL}(\cos\lambda\sinh\lambda - \sin\lambda\cosh\lambda) - \\ &\frac{\lambda^3 I_{bf}}{mL^3}(\cosh\lambda\sin\lambda + \sinh\lambda\cos\lambda) + \frac{\lambda^4 M_{bf} I_{bf}}{m^2 L^4}(1 - \cos\lambda\cosh\lambda) = 0, \end{aligned} \tag{A3}$$

where M_{bf} and I_{bf} are the mass and the moment of inertia of the bluff body. In addition, the modal coefficient C_r of the rth mode satisfies the following orthogonality conditions

$$\int_0^L \varphi_s(x) m \varphi_r(x) dx + \varphi_s(L) M_{bf} \varphi_r(L) + \left[\frac{d\varphi_s(x)}{dx} I_{bf} \frac{d\varphi_r(x)}{dx}\right]_{x=L} = \delta_{rs}, \tag{A4}$$

$$\int_0^L \varphi_s(x) E_b I_b \frac{d^4\varphi_r(x)}{dx^4} dx - \left[\varphi_s(x) E_b I_b \frac{d^3\varphi_r(x)}{dx^3}\right]_{x=L} + \left[\frac{d\varphi_s(x)}{dx} E_b I_b \frac{d^2\varphi_r(x)}{dx^2}\right]_{x=L} = \omega_r^2 \delta_{rs}, \tag{A5}$$

where δ_{rs} represents the Kronecker delta.

Appendix B. Structural parameters in theoretical analysis

Table B1

Table B1
Structural parameters in theoretical analysis.

Parameter	Value	Parameter	Value
Beam density	2700 kg/m^3	Bluff body length	50 mm
Young's modulus	69 GPa	Bluff body width	30 mm
Beam length	237 mm	Bluff body height	80 mm
Beam width	19.5 mm	Flag width	80 mm
Beam thickness	0.6 mm	Distance from flag center to base	125 mm
Bluff body mass	4.1 g		

Appendix C. Galloping suppression versus system modal frequencies and galloping force

For a given galloping system, system parameters remain constant. However, to validate the correlation between characteristic galloping suppression frequencies and structural modal frequencies, the beam thickness is adjusted to alter modal frequencies. The galloping suppression performance relative to flag fluttering frequency and force amplitude is analyzed. As shown in Fig. C1**(a)**, when the beam thickness is 0.8 mm, the second and third modal frequencies of the beam increase to 56.1 Hz and 166.7 Hz, respectively, with the corresponding characteristic galloping suppression frequencies being close to 59 Hz and 169 Hz. Similarly, as illustrated in Fig. C1**(b)**, increasing beam thickness to 1 mm shifts these characteristic frequencies to 74 Hz and 207 Hz, respectively, confirming their alignment with the second and third modal frequencies. As summarized in Table C1, the critical galloping suppression force increases slightly from 5 N/m to 7.7 N/m for an excitation at f_{r2}. Conversely, the critical force for f_{r3} exhibits greater sensitivity to structural parameters, rising sharply from 27 N/m to 96 N/m. Effective suppressions at f_{r3} require careful tuning of force amplitude based on structural characteristics.

Table C1
Characteristic frequencies and corresponding critical force values for galloping suppression with different beam thicknesses.

Beam thickness	Characteristic frequency f_{c2}	Critical force	Characteristic frequency f_{c3}	Critical force
0.6 mm	45 Hz	5 N/m	124 Hz	27 N/m
0.8 mm	59 Hz	7 N/m	169 Hz	52 N/m
1 mm	74 Hz	7.7 N/m	207 Hz	96 N/m

In a given galloping system, the geometry of the bluff body remains constant but directly affects galloping intensity according to Eq. (3). To provide a more comprehensive analysis, the normalized bluff body height ($H_{bfu} = H_{bf}/L$) is adjusted to explore the suppression performance under different galloping force. As shown in Fig. C1**(c)**, the injection of a 45 Hz excitation results in a slight increase in the lower critical galloping suppression force as the bluff body height increases. Additionally, a broader suppression bandwidth is achieved. Conversely, with a 124 Hz excitation, as shown in Fig. C1 **(d)**, the lower critical force first decreases to a minimum with a H_{bfu} of 0.29 before increasing again. Notably, when H_{bfu} is around 0.29, the suppressed galloping amplitude exhibits a slight increase with a larger force.

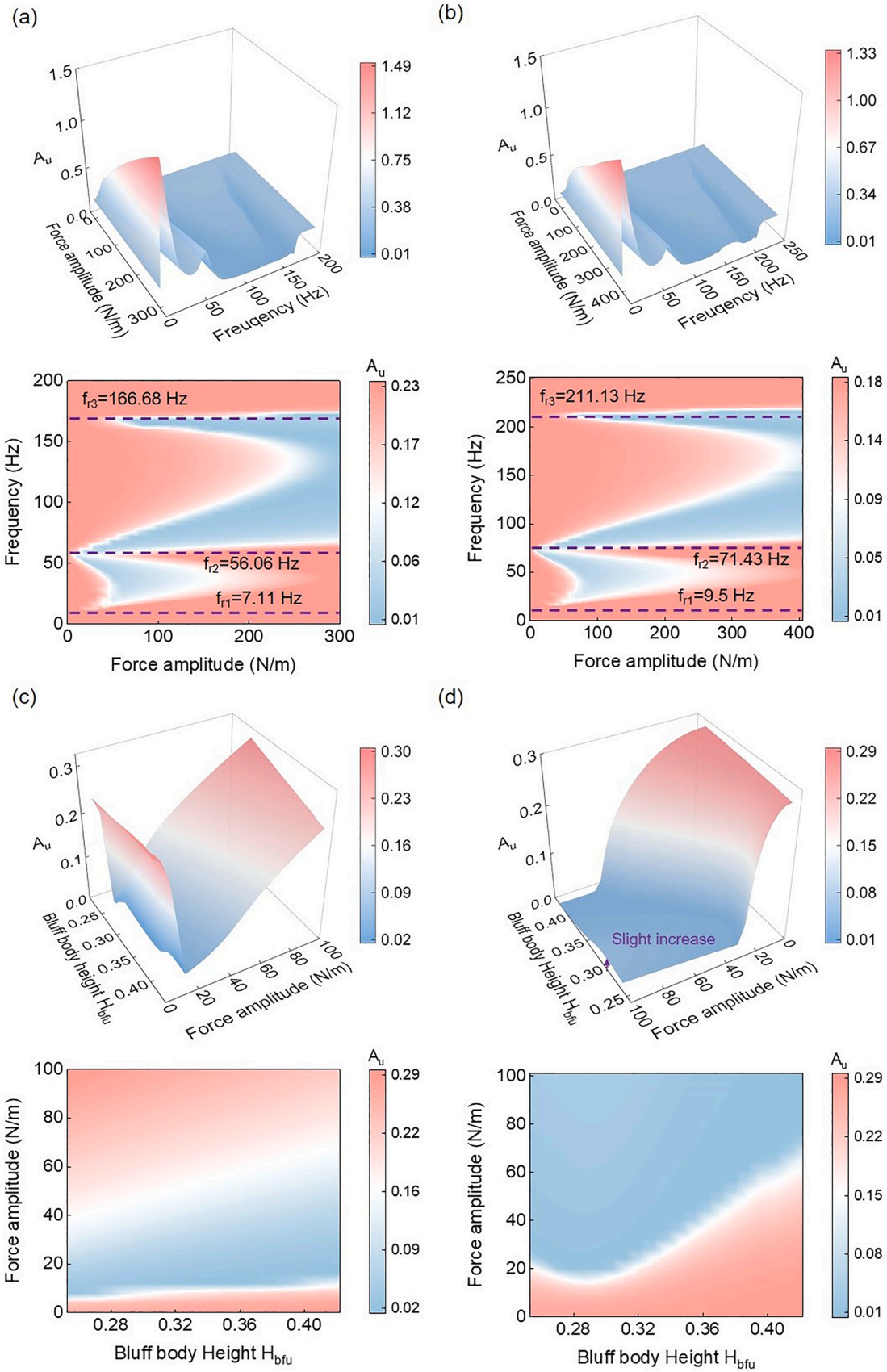

Fig. C1. Galloping suppression versus system modal frequencies and system galloping force. (a) Three-dimensional and their two-dimensional views of galloping amplitude versus flag fluttering frequency and force amplitude with beam thicknesses of 0.8 mm and (b) 1 mm at 6 m/s. The purple dashed lines indicate the first three modal frequencies of the system. (c) Three-dimensional and their two-dimensional views of galloping amplitude versus bluff body height and force amplitude with excitations at 45 Hz and (d) 124 Hz at 6 m/s.

Data availability

Data will be made available on request.

References

[1] Wang E, Zhao S, Xu W, Xiao Q, Li B. Effect of splitter plate length on FIV of circular cylinder. Int. J. Mech. Sci. 2023;254:108413.
[2] Lau YL, So RMC, Leung RCK. Flow-induced vibration of elastic slender structures in a cylinder wake. J. Fluids. Struct. 2004;19(8):1061–83.
[3] Parameshwaran R, Dhulipalla SJ, Yendluri DR. Fluid-structure interactions and flow induced vibrations: a review. Procedia Eng. 2016;144:1286–93.
[4] Owen JC, Bearman PW, Szewczyk AA. Passive control of VIV with drag reduction. J. Fluids. Struct. 2001;15(3–4):597–605.
[5] Wang J, Zhang Y, Liu M, Hu G. Etching metasurfaces on bluff bodies for vortex-induced vibration energy harvesting. Int. J. Mech. Sci. 2023;242:108016.
[6] Zhang M, Song Y, Abdelkefi A, Yu H, Wang J. Vortex-induced vibration of a circular cylinder with nonlinear stiffness: prediction using forced vibration data. Nonlinear. Dyn. 2022;108(3):1867–84.
[7] Eloy C, Souilliez C, Schouveiler L. Flutter of a rectangular plate. J. Fluids. Struct. 2007;23(6):904–19.
[8] Tian K, Wang Y, Cao D, Yu K. Approximate global mode method for flutter analysis of folding wings. Int. J. Mech. Sci. 2024;265:108902.
[9] Watanabe Y, Suzuki S, Sugihara M, Sueoka Y. An experimental study of paper flutter. J. Fluids. Struct. 2002;16(4):529–42.
[10] Xu C, Zhao L. Investigation on the characteristics of a novel internal resonance galloping oscillator for concurrent aeroelastic and base vibratory energy harvesting. Mech. Syst. Signal. Process. 2022;173:109022.
[11] Li HT, Ren H, Cao F, Qin WY. Improving the galloping energy harvesting performance with magnetic coupling. Int. J. Mech. Sci. 2023;237:107785.
[12] Zhao L. Synchronization extension using a bistable galloping oscillator for enhanced power generation from concurrent wind and base vibration. Appl. Phys. Lett. 2020;116(5):053904.
[13] Tang B, Fan X, Wang J, Tan W. Suppression of wake-induced galloping of tandem cylinders by helical strakes. Int. J. Mech. Sci. 2024;273:109301.
[14] Wang J, Zhang C, Hu G, Liu X, Liu H, Zhang Z, et al. Wake galloping energy harvesting in heat exchange systems under the influence of ash deposition. Energy 2022;253:124175.
[15] Du X, Chen H, Li C, Li Z, Wang W, Guo D, et al. Wake galloping piezoelectric-electromagnetic hybrid ocean wave energy harvesting with oscillating water column. Appl. Energy 2024;353:122081.
[16] Huang L. Flutter of cantilevered plates in axial flow. J. Fluids. Struct. 1995;9(2):127–47.
[17] Pasha Zanussi V, Shahverdi H, Khalafi V, Navardi MM. Nonlinear flutter analysis of arbitrary functionally graded plates using Isogeometric approach. Thin-Walled Struct. 2023;182:110236.
[18] Dong L, Tang Q, Zhao C, Hu G, Qu S, Liu Z, et al. Flag-type hybrid nanogenerator utilizing flapping wakes for consistent high performance over an ultra-broad wind speed range. Nano Energy 2024;119:109057.
[19] Dong L, Hu G, Tang Q, Zhao C, Yang F, Yang Y. Advanced aerodynamics-driven energy harvesting leveraging galloping-flutter synergy. Adv. Funct. Mater. 2024:2414324.
[20] Chen C, J-w Zhou, Li F, Gong D. Nonlinear vortex-induced vibration of wind turbine towers: theory and experimental validation. Mech. Syst. Signal. Process. 2023;204:110772.
[21] Ma Z, Li J, Zhang X, Qiao X, Zhao G, Shen Z. Flow field characteristics analysis of vortex-induced vibration of bridge tower based on dynamic mode decomposition method. Adv. Struct. Eng. 2023;26(14):2733–48.
[22] Liu D, Ai S, Sun L, Guedes Soares C. Vortex-induced vibrations of catenary risers in varied flow angles. Int. J. Mech. Sci. 2024;269:109086.
[23] Talib E, Shin JH, Kwak MK, Koo JR. Dynamic modeling and simulation for transmission line galloping. J. Mech. Sci. Technol. 2019;33:4173–81.
[24] Ruan L, Zhu H, Hu C. A study on vortex-induced vibration of a long flexible catenary cable in perpendicular flow. Ocean Eng. 2024;305:117937.
[25] Chen WL, Sun S, Yang W. Multi-mode vortex-induced vibration of a long-span bridge under non-uniform flows. Mech. Syst. Signal. Process. 2023;185:109800.
[26] Yan WJ, Feng ZQ, Yang W, Yuen KV. Bayesian inference for the dynamic properties of long-span bridges under vortex-induced vibration with Scanlan's model and dense optical flow scheme. Mech. Syst. Signal. Process. 2022;174:109078.
[27] Avila-Sanchez S, Lopez-Garcia O, Cuerva A, Meseguer J. Assesment of the transverse galloping stability of a railway overhead located above a railway bridge. Int. J. Mech. Sci. 2017;131-132:649–62.
[28] Tsai LW, Alipour A. Studying the wind-induced vibrations of a traffic signal structure through long term health monitoring. Eng. Struct. 2021;247:112837.
[29] Païdoussis MP. Real-life experiences with flow-induced vibration. J. Fluids. Struct. 2006;22(6):741–55.
[30] Zhang C, Tang G, Lu L, Jin Y, An H, Cheng L. Flow-induced vibration of two tandem square cylinders at low Reynolds number: transitions among vortex-induced vibration, biased oscillation and galloping. J. Fluid. Mech. 2024;986:A10.
[31] Tian H, Yurchenko D, Li Z, Guo J, Kang X, Wang J. Dumbbell-shaped piezoelectric energy harvesting from coupled vibrations. Int. J. Mech. Sci. 2024;281:109681.
[32] Zhao C, Hu G, Yang Y. A cantilever-type vibro-impact triboelectric energy harvester for wind energy harvesting. Mech. Syst. Signal. Process. 2022;177:109185.
[33] Hnin T, Yagi T, Noguchi K, Pradhan M, Kyotani R, Matsumiya H. Aerodynamic interaction between galloping instability and vortices in corner-cut rectangular cylinders. J. Fluids. Struct. 2024;127:104108.
[34] Siriyothai P, Kittichaikarn C. Performance enhancement of a galloping-based energy harvester with different groove depths on square bluff body. Renew. Energy 2023;210:148–58.
[35] Wang J, Tang L, Zhao L, Zhang Z. Efficiency investigation on energy harvesting from airflows in HVAC system based on galloping of isosceles triangle sectioned bluff bodies. Energy 2019;172:1066–78.
[36] Chen W, Zhao Y, Ji C, Srinil N, Song L. Experimental observation of flow-induced vibrations of a transversely oscillating D-section prism. Phys. Fluids 2021;33(9).
[37] Agarwal A, Purohit A. Study of vibration modes and strain distribution of a flow energy harvester in the wake region of different bluff bodies. Proc. Inst. Mech. Eng. Part C 2021;235(22):5994–6008.
[38] Païdoussis MP, Price SJ, De Langre E. Fluid-structure interactions: cross-flow-induced instabilities. Cambridge University Press; 2010.
[39] Wang J, Geng L, Zhou S, Zhang Z, Lai Z, Yurchenko D. Design, modeling and experiments of broadband tristable galloping piezoelectric energy harvester. Acta Mechanica Sinica 2020;36(3):592–605.
[40] Wang J, Zhao L. Toward nonlinear galloping energy harvesting interfaced with different power extraction circuits. IEEE/ASME Trans. Mechatr. 2022;27(5):2678–89.
[41] Vinod A, Auvil A, Banerjee A. On passive control of transition to galloping of a circular cylinder undergoing vortex induced vibration using thick strips. Ocean Eng. 2018;163:223–31.
[42] Ran Y, Deng Z, Yu H, Chen W, Gao D. Review of passive control of flow past a circular cylinder. J. Vis. 2023;26(1):1–44.
[43] Guo H, Liu B, Yu Y, Cao S, Chen Y. Galloping suppression of a suspended cable with wind loading by a nonlinear energy sink. Arch. Appl. Mech. 2017;87(6):1007–18.
[44] Qu S, Ding W, Dong L, Zhu J, Zhu S, Yang Y, et al. Chiral phononic crystal-inspired railway track for low-frequency vibration suppression. Int. J. Mech. Sci. 2024:109275.
[45] Ding W, Chen T, Yu D, Chen C, Zhang R, Zhu J, et al. Isotacticity in chiral phononic crystals for low-frequency bandgap. Int. J. Mech. Sci. 2024;261:108678.
[46] Xing J, Rezaei M, Dai H, Liao WH. Suppressing galloping-induced vibrations by integrating bluff body with surface protrusions. AIP. Adv. 2024;14(2):025236.
[47] Zhao S, Zhang H, Zhang C, Zhang Y. Anti-galloping effect of the catenary positive feeder air flow spoiler in strong wind areas of Lanzhou–Urumqi High-speed Railway. J. Appl. Sci. Eng. 2021;25(4):799–812.
[48] Katsuchi H, Yamada H, Sakaki I, Okado E. Wind-tunnel investigation of the aerodynamic performance of surface-modification cables. Engineering 2017;3(6):817–22.
[49] Matsumiya H, Yukino T, Shimizu M, Nishihara T. Field observation of galloping on four-bundled conductors and verification of countermeasure effect of loose spacers. J. Wind Eng. Indus. Aerodyn. 2022;220:104859.
[50] Taruishi S, Matsumiya H. Investigation of effect of galloping countermeasures for four-bundled conductors through field observations. Cold. Reg. Sci. Technol. 2023;214:103962.
[51] Abdel-Rohman M. Design of tuned mass dampers for suppression of galloping in tall prismatic structures. J. Sound. Vib. 1994;171(3):289–99.
[52] Wang L, Zhou Y, Nagarajaiah S, Shi W. Bi-directional semi-active tuned mass damper for torsional asymmetric structural seismic response control. Eng. Struct. 2023;294:116744.
[53] Balendra T, Wang C, Cheong H. Effectiveness of tuned liquid column dampers for vibration control of towers. Eng. Struct. 1995;17(9):668–75.
[54] Domizio M, Ambrosini D, Campi A. A novel tuned liquid damper for vibration control in high-frequency structures. Eng. Struct. 2024;301:117350.
[55] Egger P, Caracoglia L. Analytical and experimental investigation on a multiple-mass-element pendulum impact damper for vibration mitigation. J. Sound. Vib. 2015;353:38–57.
[56] Akbar MA, Wong WO, Rustighi E. Design optimization of a single-mass impact damper. J. Sound. Vib. 2024;570:118019.
[57] Gagnon L, Morandini M, Ghiringhelli GL. A review of particle damping modeling and testing. J. Sound. Vib. 2019;459:114865.
[58] Lu Z, Wang Z, Masri SF, Lu X. Particle impact dampers: past, present, and future. Struct. Control Health Monitor. 2018;25(1):e2058.
[59] Hsieh MC, Huang GL, Liu H, Chen SJ, Chen BF. A numerical study of hybrid tuned mass damper and tuned liquid damper system on structure motion control. Ocean Eng. 2021;242:110129.
[60] Chesné S, Inquieté G, Cranga P, Legrand F, Petitjean B. Innovative hybrid mass damper for dual-loop controller. Mech. Syst. Signal. Process. 2019;115:514–23.
[61] Liu Q, Cao J, Zhang Y, Zhao Z, Kerschen G, Jing X. Interpretable sparse identification of a bistable nonlinear energy sink. Mech. Syst. Signal. Process. 2023;193:110254.
[62] Dai HL, Yang YW, Abdelkefi A, Wang L. Nonlinear analysis and characteristics of inductive galloping energy harvesters. Commun. Nonlinear Sci. Numer. Simul. 2018;59:580–91.
[63] Zhang Z, Lu ZQ, Ding H, Chen LQ. An inertial nonlinear energy sink. J. Sound. Vib. 2019;450:199–213.
[64] Fang S, Chen K, Xing J, Zhou S, Liao WH. Tuned bistable nonlinear energy sink for simultaneously improved vibration suppression and energy harvesting. Int. J. Mech. Sci. 2021;212:106838.
[65] Liao X, Chen L, Lee H. A customizable cam-typed bistable nonlinear energy sink. Int. J. Mech. Sci. 2024;271:109305.

[66] Lou W, Huang C, Huang M, Liang H, Yu J. Galloping suppression of iced transmission lines by viscoelastic-damping interphase spacers. J. Eng. Mech. 2020; 146(12):04020135.
[67] Duan F, Song Y, Gao S, Liu Y, Chu W, Lu X, et al. Study on aerodynamic instability and galloping response of rail overhead contact line based on wind tunnel tests. IEEe Trans. Veh. Technol. 2023;72(6):7211–20.
[68] Zhang Z, Han Y, Yu J, Hu P, Cai CS. Anti-galloping analysis of iced quad bundle conductor based on compound damping cables. Eng. Struct. 2024;306:117831.
[69] Dai HL, Abdelkefi A, Wang L. Usefulness of passive non-linear energy sinks in controlling galloping vibrations. Int. J. Non. Linear. Mech. 2016;81:83–94.
[70] Selwanis MM, Franzini GR, Béguin C, Gosselin FP. Wind tunnel demonstration of galloping mitigation with a purely nonlinear energy sink. J. Fluids. Struct. 2021; 100:103169.
[71] Selwanis MM, Franzini GR, Béguin C, Gosselin FP. Multi-ball rotative nonlinear energy sink for galloping mitigation. J. Sound. Vib. 2022;526:116744.
[72] Franzini GR, Maciel VSF, Vernizzi GJ, Zulli D. Simultaneous passive suppression and energy harvesting from galloping using a bistable piezoelectric nonlinear energy sink. Nonlinear. Dyn. 2023;111(24):22215–36.
[73] Oliva M, Barone G, Lo Iacono F, Navarra G. Nonlinear energy sink and Eurocode 8: an optimal design approach based on elastic response spectra. Eng. Struct. 2020; 221:111020.
[74] Li X, Ding H, Chen LQ. Effects of weights on vibration suppression via a nonlinear energy sink under vertical stochastic excitations. Mech. Syst. Signal. Process. 2022; 173:109073.
[75] Peng J, Li Y, Li L, Lenci S, Sun H. Time-delay feedback control of a suspended cable driven by subharmonic and superharmonic resonance. Chaos Solitons Fractals 2024;181:114646.
[76] Dai HL, Abdelkefi A, Wang L, Liu WB. Time-delay feedback controller for amplitude reduction in vortex-induced vibrations. Nonlinear. Dyn. 2015;80(1): 59–70.
[77] Li G, Li L, Zhu P. Galloping control for iced conductors using tuned mass dampers with fixed time-delayed feedback. Shock Vib. 2019;(1):4823457.
[78] Chizhevsky VN, Smeu E, Giacomelli G. Experimental evidence of ``vibrational resonance'' in an optical system. Phys. Rev. Lett. 2003;91(22):220602.
[79] Abusoua A, Daqaq MF. Changing the nonlinear resonant response of an asymmetric mono-stable oscillator by injecting a hard high-frequency harmonic excitation. J. Sound. Vib. 2018;436:262–72.
[80] Yan Z, Liu X. Fractional-order harmonic resonance in a multi-frequency excited fractional Duffing oscillator with distributed time delay. Commun. Nonlinear Sci. Numer. Simul. 2021;97:105754.
[81] Ullner E, Zaikin A, García-Ojalvo J, Báscones R, Kurths J. Vibrational resonance and vibrational propagation in excitable systems. Phys. Lett. A 2003;312(5): 348–54.
[82] Alhadidi AH, Khazaaleh S, Daqaq MF. Suppression of galloping oscillations by injecting a high-frequency excitation. Philos. Trans. R. Soc. A 2021;379(2198): 20200244.
[83] Sahoo PK, Chatterjee S. Nonlinear dynamics and control of galloping vibration under unsteady wind flow by high-frequency excitation. Commun. Nonlinear Sci. Numer. Simul. 2023;116:106897.
[84] Daqaq MF, Alhadidi AH, Khazaaleh S. Suppression of structural galloping by applying a harmonic base excitation at certain frequencies. Nonlinear. Dyn. 2022; 110(4):3001–14.
[85] Zhao L, Yang Y. An impact-based broadband aeroelastic energy harvester for concurrent wind and base vibration energy harvesting. Appl. Energy 2018;212: 233–43.
[86] Connell BSH, Yue DKP. Flapping dynamics of a flag in a uniform stream. J. Fluid. Mech. 2007;581:33–67.
[87] Tang L, Zhao L, Yang Y, Lefeuvre E. Equivalent circuit representation and analysis of galloping-based wind energy harvesting. IEEE/ASME Trans. Mechatronics 2015; 20(2):834–44.
[88] Dong L, Hu G, Zhang Y, Ding W, Qu S, Tang Q, et al. Metasurface-enhanced multifunctional flag nanogenerator for efficient wind energy harvesting and environmental sensing. Nano Energy 2024;124:109508.
[89] Wang Y, Yang E, Chen T, Wang J, Hu Z, Mi J, et al. A novel humidity resisting and wind direction adapting flag-type triboelectric nanogenerator for wind energy harvesting and speed sensing. Nano Energy 2020;78:105279.
[90] Zhang Y, Fu SC, Chan KC, Shin DM, Chao CYH. Boosting power output of flutter-driven triboelectric nanogenerator by flexible flagpole. Nano Energy 2021;88: 106284.
[91] Gallegos RKB, Sharma RN. Small flags in rectangular channels: dynamics and mean wake characteristics. Int. J. Mech. Sci. 2019;155:518–35.
[92] Erturk A, Inman DJ. On mechanical modeling of cantilevered piezoelectric vibration energy harvesters. J. Intell. Mater. Syst. Struct. 2008;19(11):1311–25.